INFLUENCE OF WIND ON THE NOISE FOOTPRINT OF A HELICOPTER LANDING

W.F.J. Olsman[1] and M. Lummer[2]

[1]DLR in der Helmholtz-Gemeinschaft Institute of Aerodynamics and Flow Technology, Helicopter Division, Lilienthalplatz 7, 38108 Braunschweig, Germany
[2]DLR in der Helmholtz-Gemeinschaft Institute of Aerodynamics and Flow Technology, Technical Acoustics Division, Lilienthalplatz 7, 38108 Braunschweig, Germany

Abstract

Noise constraints is one of the limiting factors for helicopter operation. It is therefore necessary to minimise the perceived noise on the ground. This can be achieved by modification of the flight path of the helicopter in such a way that noise intense flight conditions are avoided and noise is redistributed to less noise sensitive areas. The presence of wind has influence on the flight conditions of the helicopter and also on the propagation of sound from the helicopter, through the atmosphere, to the ground. To take into account the effects of wind, wind gradients and temperature gradients the computational method at DLR is extended with a ray tracing algorithm. The effects of wind are illustrated for a monopole sound source and for a complete helicopter approach with the EC135. The shape and level of the sound exposure level contours right below the flight path are mostly affected by changes in flight conditions, .i.e. changes in acoustic source. The contours further away from the flight path are mostly affected by changes in the propagation of sound. The effects of wind are most pronounced for the case of a head or side wind.

1 INTRODUCTION

Typically one of the limitations for helicopter operation is noise restriction. For this reason noise reduction of helicopters is an active research topic. One can distinguish between two approaches to reduce the noise of a helicopter, either the redesign of the helicopter (mostly the main rotor) or the design of alternative flight procedures. Due to the long life time of a typical aircraft, it will take years before the newly designed quieter helicopters have replaced the ones currently in service. The design of new procedures, however, can be implemented on a much shorter time scale. The problem of noise reduction is relevant in both civil and military applications. For civil applications the goal is to minimise annoyance, while for military applications the goal is to minimise detectability.

Within several internal projects and EU projects a computational tool has been developed at DLR to predict the flyover noise of a helicopter and to design noise abatement flight procedures[16;11;7]. Currently DLR is involved in the European Joint Technology Initiative CleanSky. Within the subtask GreenRotorCraft 5 (GRC5) the computational tool is further extended and new noise abatement flight procedures are developed. One of the extensions made to the computational tool is the ability to take into account the effects of wind, wind gradients and temperature gradients.

Up to recently the influence of wind was only taken into account by providing the flight mechanics tool with local wind velocities. However, the effect of wind on the propagation of sound through the atmosphere was not taken into account. In the past it has already been observed that the influence of wind might be important and it has been suggested to take these effects into account by a ray tracing method[11]. The presence of wind has two effects, first it will change the flight conditions, necessary to fly a predetermined flight path. Here the noise sources change due to the presence of wind. Second, wind has an influence on the propagation of sound through the atmosphere from the helicopter to the ground. Usually there exists a vertical gradient in wind velocity due to the presence of the atmospheric boundary layer. These gradients cause the acoustic wave front to bend, which can lead to appearance of a zone of silence, also known as a shadow zone, upstream of the source.

A ray tracing method for fixed wing aircraft application has been presented in the past[14]. A paper which describes the effect on the noise footprint of a head and tail wind component is given in[6]. In this paper only the convective effect of wind is taken into account. The effect of refraction due to the atmospheric boundary layer was not taken into account.

This paper is organised as follows. First in section 2 a short description of DLR's computational chain

SELENE is given. Then the ray tracing algorithm is described in section 3. The ray tracing algorithm is validated in section 4 by comparison with an analytical solution for a monopole mass injection source. The effect of flow on the noisefoot print is first demonstated by the use of a monopole. In section 5 the effect of wind on the noise footprint of an EC135 is demonstrated by use of the computational chain SELENE with the integrated ray tracing method. Finally the conclusions are presented in section 6.

2 DESCRIPTION OF COMPUTATIONAL CHAIN

DLR's software tool for helicopter noise footprint prediction is called SELENE (Sound Exposure Level starting from Evaluation of Noise Emissions) and has been used in the past to optimise helicopter approach procedures [16;7].

The computational method is based on the use of an aeroacoustic database of so called noise directivity hemispheres. A noise hemisphere is a ficticious hemisphere with fixed radius that is used to describe the noise directivity of the helicopter. The database of noise hemispheres can be obtained either by numerical computation or by flight experiments. At the moment DLR uses hemispheres that were obtained from dedicated flight experiments with the EC135-ACT/FHS and the BO105 [15]. The hemispheres in the database are stored with the corresponding value of the advance ratio of the main rotor μ, the tip path plane angle α_{TPP} and the thrust coefficient C_T. An unstructured mesh is then generated by use of a Delaunay triangulation. This mesh can be used to interpolate a hemisphere corresponding to a flight condition that was not measured. If a flight condition is encountered that is outside the measured flight envelope, a nearest neighbour search is used. The three aforementioned aerodynamic parameters are known to govern main rotor Blade Vortex Interaction (BVI) noise in steady and quasi-steady flight conditions [18;1]. The tip path plane angle is related to the vortex miss distance, the advance ratio controls the epicycloidal shape of the paths of the tip vortices and the thrust coefficient is related to the blade loading.

A typical computation of the noise footprint consists of the following steps. First the flight path is generated from user prescribed waypoints with the corresponding velocities by the use of Bezier splines. By using a Bezier spline the resulting flight path is guaranteed to lie within the convex hull of the input points, thereby avoiding oscillations between the input points. After generating the flight path initial checks can be made on the maximal acceleration, velocity etc. Prescribing the position and the velocity as a function of time is, however, not enough to fully define the flight path of the helicopter, since the yaw angle still provides a degree of freedom. Currently the yaw angle is chosen such that the fuselage is aligned with the flight direction. For the case of no wind this corresponds to flight without side slip. A time accurate simulation with a flight mechanics tool (currently HOST[2]) is then used to compute flight mechanical parameters along the flight path, such as (but not limited to) the attitude angles, thrust coefficient, advance ratio of the main rotor and tip path plane angle. After obtaining the flight mechanical parameters more complex checks on the flight path can be made, such as violations in the Height-Velocity diagram, Vortex Ring State conditions or too large values of the fuselage pitch angle. Finally the three flight mechanical parameters (μ, α_{TTP}, C_T) are used to interpolate a hemisphere from the aeroacoustic database. The attitude angles of the helicopter are used to obtain the correct orientation of the hemisphere in space and then lastly the noise of the hemisphere is propagated to the ground taking into account spherical spreading, Doppler frequency shift, wind effects, atmospheric absorption and ground reflection.

For more details about the computational method the reader is referred to previous publications [11;16;7].

3 DESCRIPTION OF RAY TRACING MODULE

The ray tracing equations are a high frequency limit of the linearized Euler equations and allow the calculation of the propagation of high frequency sound fields through a steady non-uniform mean flow field. The high frequency limit requires that the mean flow field doesn't change much over an acoustic wave length.

It should be pointed out, that the concept of moving sources does not fit well into the ray tracing approach, which is formulated in frequency space. In case of slowly moving sources, however, it seems to be justified using a quasi-steady approach, i.e., to consider the problem in a coordinate system where the source is at rest.

3.1 The ray equations

In order to derive the ray equations, one makes a wave ansatz which has for the pressure field $p(\boldsymbol{x}, t)$ the form

$$p(\boldsymbol{x}, t) = A(\boldsymbol{x}) e^{i\omega(\psi(\boldsymbol{x}) - t)}. \tag{1}$$

i is the imaginary unit, $\boldsymbol{x}$ and t are position and time, ω is the frequency, $\psi(\boldsymbol{x})$ is the phase function and $A(\boldsymbol{x})$ is an amplitude function. Amplitude and phase function will be determined by the ray tracing equations. Important is the gradient of the phase function, which is denoted by a symbol of its own[a] $\boldsymbol{\nu} = \nu_j \equiv \psi_{,j}(\boldsymbol{x})$. Substitution of the ansatz into the linearized Euler

[a] Tensor notation is used for the derivatives, i.e., one writes for the gradient $\frac{\partial(.)}{\partial x_j} = (.)_{,j}$. The length of a vector is denoted by the vector symbol without coordinate index, e.g., $\nu = \sqrt{\nu_j \nu_j}$. Einstein's summation convention applies.

equations yields in the high frequency limit $\omega \to \infty$ the so-called eikonal equation[3]

$$H(\boldsymbol{x}, \boldsymbol{\nu}) = \frac{1}{2}\left(\nu^2 - \frac{1}{c^2}\left(1 - v_i\nu_i\right)^2\right) = 0. \tag{2}$$

Here $c(\boldsymbol{x})$ is the sound speed of the mean flow field and $v_i(\boldsymbol{x})$ is the mean flow velocity. From the eikonal equation one can conclude that

$$1 - v_i\nu_i = c\nu. \tag{3}$$

Equation (2) is a partial differential equation of first order for the phase function $\psi(\boldsymbol{x})$ and can be solved by the method of characteristics, i.e., its solution can be calculated along curves $\boldsymbol{x}(\tau)$, the so-called rays. τ parameterizes these rays. Since the eikonal equation does not depend on the frequency ω the ray paths are also independent of the frequency. Applying the methods of characteristics to the eikonal equation, the ray equations become

$$\begin{aligned}
\frac{dx_i}{d\tau} &= \frac{\partial H}{\partial \nu_i} = \nu_i + \frac{\nu}{c}v_i, \\
\frac{d\nu_i}{d\tau} &= -\frac{\partial H}{\partial x_i} = -\frac{\nu}{c}\left(\nu c_{,i} + \nu_j v_{j,i}\right), \\
\frac{d\psi}{d\tau} &= \psi_{,i}\frac{dx_i}{d\tau} = \frac{\nu}{c}\left(c\nu + v_j\nu_j\right) = \frac{\nu}{c}.
\end{aligned}$$

In the last line, equation (3) was used. Introducing the group velocity c_{gi} by

$$c_{gi} \equiv v_i + c\frac{\nu_i}{\nu}$$

one can write for the ray equations

$$\begin{aligned}
\frac{dx_i}{d\tau} &= \frac{\nu}{c}c_{gi}, \\
\frac{d\nu_i}{d\tau} &= -\frac{\nu}{c}\left(\nu c_{,i} + \nu_j v_{j,i}\right), \\
\frac{d\psi}{d\tau} &= \frac{\nu}{c}.
\end{aligned}$$

It is often more convenient to use the arc length s along the ray $\boldsymbol{x}(\tau)$ as parameter for the solution of the ray equations. The differential of the arc length is defined by $ds = \sqrt{dx_j dx_j}$ and one obtains

$$ds = \sqrt{\frac{dx_j}{d\tau}\frac{dx_j}{d\tau}}d\tau = \frac{\nu}{c}c_g d\tau$$

where $c_g = \sqrt{c_{gj}c_{gj}}$. The ray equations then become

$$\dot{x}_i \equiv \frac{dx_i}{ds} = \frac{c_{gi}}{c_g}, \tag{4}$$

$$\dot{\nu}_i \equiv \frac{d\nu_i}{ds} = -\frac{\nu c_{,i} + \nu_j v_{j,i}}{c_g}, \tag{5}$$

$$\dot{\psi} \equiv \frac{d\psi}{ds} = \frac{1}{c_g}. \tag{6}$$

The ray path is determined by the ordinary differential equations (4-5). Besides the eikonal equation, one obtains for the pressure amplitude $A(\boldsymbol{x}(s))$ along the ray the relation

$$\frac{A^2 D}{c^2\rho\nu^2} = const.,$$

cf.[3]. Where $\rho(\boldsymbol{x})$ denotes the mean flow density and $D(\boldsymbol{x})$ stands for the Jacobian of the rays, i.e., a measure for the volume element made from infinitesimal neighbouring rays. It can be expressed using the ray coordinates by

$$D(s;\alpha,\beta) = \frac{d\boldsymbol{x}}{ds}\cdot\left(\frac{\partial \boldsymbol{x}}{\partial\alpha}\times\frac{\partial\boldsymbol{x}}{\partial\beta}\right) \tag{7}$$

where α and β are parameters of the ray field. The ratio of the pressure amplitude at a target point s_1 and a reference point s_0 is then

$$\frac{|p(s_1)|}{|p(s_0)|} = \frac{A(s_1)}{A(s_0)} = \sqrt{\left[\frac{D}{c^2\rho\nu^2}\right]_{s=s_0}\left[\frac{c^2\rho\nu^2}{D}\right]_{s=s_1}}.$$

In order to calculate the Jacobian $D(s;\alpha,\beta)$, cf. equation (7), along a ray it is convenient to have a differential equation for it. One can denote the partial derivatives with respect to the parameters α, β by suffixes[b] and obtain for the derivative of the Jacobian with respect to the arc length s

$$\dot{D} = \ddot{\boldsymbol{x}}\cdot(\boldsymbol{x}_{,\alpha}\times\boldsymbol{x}_{,\beta}) + \dot{\boldsymbol{x}}\cdot(\dot{\boldsymbol{x}}_{,\alpha}\times\boldsymbol{x}_{,\beta}) + \dot{\boldsymbol{x}}\cdot(\boldsymbol{x}_{,\alpha}\times\dot{\boldsymbol{x}}_{,\beta}).$$

For the numerical integration of this equation additional derivatives are necessary. One obtains by differentiation from the ray equations (4 -5)

$$\begin{aligned}
\ddot{x}_i &= \frac{\dot{c}_{gi}}{c_g} - \frac{c_{gj}\dot{c}_{gj}}{c_g^2}\dot{x}_i, \\
\dot{x}_{i,\alpha} &= \frac{c_{gi,\alpha}}{c_g} - \frac{c_{gj}c_{gj,\alpha}}{c_g^2}\dot{x}_i, \\
\dot{\nu}_{i,\alpha} &= -\frac{\nu_{,\alpha}c_{,i} + \nu_{j,\alpha}v_{j,i} + (\nu c_{,ik} + \nu_j v_{j,ik})x_{k,\alpha}}{c_g} - \\
&\quad - \frac{c_{gj}c_{gj,\alpha}}{c_g^2}\dot{\nu}_i.
\end{aligned}$$

Differentiation of the group velocity and the phase gradient yields

$$\begin{aligned}
\dot{c}_{gi} &= \left(v_{i,j} + c_{,j}\frac{\nu_i}{\nu}\right)\dot{x}_j + c\left(\frac{\dot{\nu}_i}{\nu} - \frac{\dot{\nu}_j\nu_j\nu_i}{\nu^3}\right), \\
c_{gi,\alpha} &= \left(v_{i,j} + c_{,j}\frac{\nu_i}{\nu}\right)x_{j,\alpha} + c\left(\frac{\nu_{i,\alpha}}{\nu} - \frac{\nu_{j,\alpha}\nu_j\nu_i}{\nu^3}\right), \\
\nu_{,\alpha} &= \frac{\nu_j\nu_{j,\alpha}}{\nu}.
\end{aligned}$$

[b] Especially one can write for the derivative of a vector $\boldsymbol{x} = x_i$

$$\frac{\partial x_i}{\partial\alpha} = \frac{\partial\boldsymbol{x}}{\partial\alpha} = \boldsymbol{x}_{,\alpha} = x_{i,\alpha}$$

Now, one has to solve an initial value problem of first order ordinary differential equations for the functions

$$\boldsymbol{x}(s;\alpha,\beta),\ \boldsymbol{\nu}(s;\alpha,\beta),\ D(s;\alpha,\beta),\ \psi(s;\alpha,\beta),$$
$$\boldsymbol{x}_{,\alpha} \equiv \frac{\partial \boldsymbol{x}(s;\alpha,\beta)}{\partial \alpha}, \quad \boldsymbol{x}_{,\beta} \equiv \frac{\partial \boldsymbol{x}(s;\alpha,\beta)}{\partial \beta},$$
$$\boldsymbol{\nu}_{,\alpha} \equiv \frac{\partial \boldsymbol{\nu}(s;\alpha,\beta)}{\partial \alpha}, \quad \boldsymbol{\nu}_{,\beta} \equiv \frac{\partial \boldsymbol{\nu}(s;\alpha,\beta)}{\partial \beta}.$$

Thus the ray tracing equations require as initial conditions for some initial value $s = s_0$ phase and phase gradient on a surface $\boldsymbol{x}(s = s_0;\alpha,\beta)$. This must be provided by an appropriate description of the acoustic source.

In case of a point source it is possible to chose the spherical polar angles angles φ and ϑ as parameters α and β. Then, the initial value for $\boldsymbol{x}(s;\varphi,\vartheta)$ is the source position and one has $\boldsymbol{x}_{,\varphi}(s = s_0) = \boldsymbol{x}_{,\vartheta}(s = s_0) = 0$.

3.2 Initial Conditions

The determination of initial conditions is demonstrated for a monopole in constant mean flow and located in the origin. Its pressure field $p(\boldsymbol{x},t)$ can be written in the form (see, e.g.[12])

$$p(\boldsymbol{x},t) = \frac{B}{f} e^{i\frac{\omega}{c_\infty}\left(\frac{f - M_f x}{\gamma^2} - c_\infty t\right)},$$
$$f = \sqrt{x^2 + \gamma^2(y^2+z^2)}, \quad \gamma^2 = 1 - M_f^2$$

where B is the pressure amplitude, c_∞ the (constant) sound speed, and M_f the flow Mach number. Comparison with equation (1) yields for phase and amplitude

$$\psi(\boldsymbol{x}) = \frac{1}{c_\infty}\frac{f - M_f x}{\gamma^2}, \quad A(\boldsymbol{x}) = \frac{B}{f}.$$

The gradient of the phase function and its length is

$$\nu_i \equiv \psi_{,i} = \frac{1}{c_\infty \gamma^2}\begin{pmatrix} \frac{x}{f} - M_f \\ \frac{\gamma^2 y}{f} \\ \frac{\gamma^2 z}{f} \end{pmatrix},$$
$$\nu \equiv \sqrt{\nu_i \nu_i} = \frac{1}{c_\infty}\frac{1}{\gamma^2}\left(1 - \frac{M_f x}{f}\right).$$

Spherical coordinates (r,φ,ϑ) can be introduced by

$$\begin{pmatrix} x \\ y \\ z \end{pmatrix} = r \begin{pmatrix} \cos\varphi \sin\vartheta \\ \sin\varphi \sin\vartheta \\ \cos\vartheta \end{pmatrix}$$

leading to

$$\nu_i = \frac{1}{c_\infty \gamma^2}\begin{pmatrix} f\cos\varphi\sin\vartheta - M_f \\ \gamma^2 f \sin\varphi \sin\vartheta \\ \gamma^2 f \cos\vartheta \end{pmatrix},$$
$$f = (\cos^2\varphi \sin^2\vartheta + \gamma^2(\sin^2\varphi\sin^2\vartheta + \cos^2\vartheta))^{-1/2},$$
$$\nu = \frac{1}{c_\infty \gamma^2}\left(1 - M_f f \cos\varphi \sin\vartheta\right)$$

In order to calculate initial conditions for the Jacobian of the rays, one needs the derivatives of the phase gradient

$$\nu_{i,\varphi} = \frac{f^3}{c_\infty}\sin\vartheta \begin{pmatrix} -\sin\varphi \\ \cos\varphi(1 - M_f^2\cos^2\vartheta) \\ M^2\cos\varphi\sin\varphi\cos\vartheta\sin\vartheta \end{pmatrix},$$
$$\nu_{i,\vartheta} = \frac{f^3}{c_\infty}\begin{pmatrix} \cos\varphi\cos\vartheta \\ \gamma^2\sin\varphi\cos\vartheta \\ -\sin\vartheta(1 - M_f^2\sin^2\varphi) \end{pmatrix}.$$

3.3 The Shooting Procedure

Usually, one is interested in the sound pressure at certain target points $\boldsymbol{x}_T$ in space. Since the ray path is the solution of a system of ordinary differential equations, equations (4-5), it depends nonlinearily on the initial conditions, i.e., the acoustic source.

The ray path can be assumed as function of the arc length s in the target point and the initial parameters α and β, i.e., $\boldsymbol{x}(s;\alpha,\beta)$. The system of nonlinear equations can then be written in the form $\boldsymbol{x}_T - \boldsymbol{x}(s;\alpha,\beta) = 0$. This system of 3 equations for 3 unknowns can be solved by a Newton procedure. The Jacobian can be calculated by first order finite differences.

3.4 The atmosphere model

The atmosphere is modeled by a simple three layer model consisting of

- the Prandtl layer in the range $z < z_P$,
- the Ekman layer in the range $z_P < z < z_E$,
- and the free atmosphere for $z_E < z$.

z denotes the height above the ground, z_P is the height of the Prandtl layer, and z_E is the upper rim of the Ekman layer. The details of this layer model can be found in[5]. Here only a very brief collection of the used formulas will be given. In the derivation presented in[5] a coordinate system is chosen whose x-axis is parallel to the so-called geostrophic wind, i.e., the wind at the upper rim of the Ekman layer. That means that due to the change of the wind direction in the Ekman layer (Ekman spiral), the wind at the ground has a component in y-direction, i.e., it is rotated by the angle ψ_E towards the y-axis. A sketch can be found in figure 1.

The main parameters of the atmosphere model are:

U_{10}	Wind velocity at $z = z_a = 10m$
φ_W	Wind direction
z_0	surface roughness
$\frac{z_P}{z_E}$	Ratio of height of Prandtl and Ekman layer
ψ_E	Ekman angle
$\gamma_{P,E,F}$	Temperature gradient inside each layer

The velocity profiles in the Prandtl and Eckman layer are now be matched at $z = z_P$ in order to obtain a continuous velocity field.

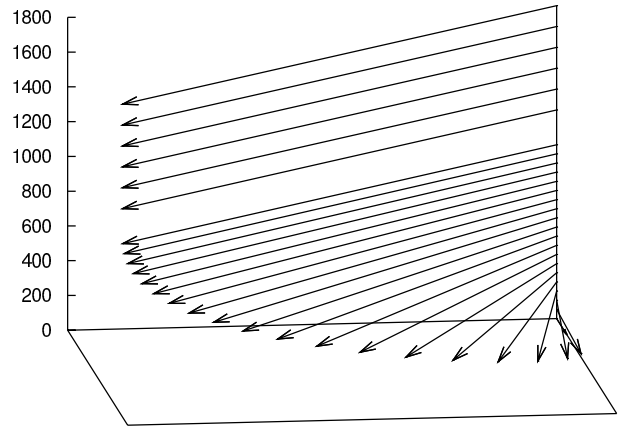

Figure 1: Sketch of the three layers in the atmospheric model. Near the bottom the wind profile is logarithmic (Prandlt layer), then a spiral effect appears (Eckman layer) and finally the wind velocity is constant (free atmosphere).

3.4.1 The Prandtl layer

Assuming a coordinate system where the x-axis is aligned with the geostrophic wind, the velocity profile in the Prandtl layer is the logarithmic boundary layer profile in the form

$$\boldsymbol{u}_P = \frac{u^*}{\kappa} \ln \frac{z+z_0}{z_0} \begin{pmatrix} \cos\psi_E \\ \sin\psi_E \end{pmatrix}, \tag{8}$$

$$u_P = |\boldsymbol{u}_P| = \frac{u^*}{\kappa} \ln \frac{z+z_0}{z_0}.$$

The velocity is 0 for $z = 0$. u^* is the wall friction velocity and $\kappa = 0.41$ is the von Kármán constant. z_0 is a measure for the surface roughness of the ground. It is usually small and set to $z_0 = 0.1$ m according to the german guide-line TA-Luft[4] for airports. The wall friction velocity is calculated from the measured wind velocity U_{10} at $z_a = 10$ m

$$u^* = \frac{\kappa U_{10}}{\ln \frac{z_a+z_0}{z_0}}.$$

The height z_P of the Prandtl layer is calculated from the height of the Ekman layer by multiplication with the fixed ratio $\frac{z_P}{z_E} = \frac{1}{40}$. The height z_E of the Ekman layer will be calculated in the next section.

The coefficient K_m of the turbulent diffusion in the Prandtl layer is assumed to be a linear function of the height

$$K_m = \kappa u^* z.$$

3.4.2 The Ekman layer

The velocity profile in the Ekman layer $z_P < z < z_E$ is assumed to be[8;5]

$$\boldsymbol{u}_E = \boldsymbol{F}\boldsymbol{u}_g \tag{9}$$

where $\boldsymbol{u}_g$ is the vector of the geostrophic wind and $\boldsymbol{F}$ the matrix

$$\boldsymbol{F} = \begin{pmatrix} 1 & 0 \\ 0 & 1 \end{pmatrix} - \sqrt{2} e^{-\frac{z-z_P}{D_E}} \sin\psi_E \begin{pmatrix} \cos\chi & \sin\chi \\ -\sin\chi & \cos\chi \end{pmatrix}$$

$$\chi \equiv \frac{z-z_P}{D_E} + \frac{\pi}{4} - \psi_E.$$

If a coordinate system is assumed where the geostrophic wind vector is aligned to the x-axis it has the form

$$\boldsymbol{u}_g = u_g \begin{pmatrix} 1 \\ 0 \end{pmatrix}. \tag{10}$$

The absolute value of the geostrophic wind velocity u_g is now determined by matching of Ekman and Prandtl layer. The velocity profile equation (9) in the Ekman layer $z_P < z < z_E$ becomes

$$\boldsymbol{u}_E(z) = u_g \begin{pmatrix} 1 - \sqrt{2} e^{-\frac{z-z_P}{D_E}} \sin\psi_E \cos\chi \\ \sqrt{2} e^{-\frac{z-z_P}{D_E}} \sin\psi_E \sin\chi \end{pmatrix}. \tag{11}$$

where u_g is the velocity of the geostrophic wind. The Ekman length D_E is connected with the diffusion coefficient K_m in the Ekman layer by the relation

$$D_E = \sqrt{2\frac{K_m}{f_c}}, \quad f_c = 10^{-4}.$$

f_c is a Coriolis parameter and has the dimension s^{-1}. K_m is assumed to be constant inside the Ekman layer and the continuity of K_m at the interface between the Prandtl and Ekman layer requires

$$D_E = \sqrt{2\frac{\kappa u^* z_P}{f_c}}.$$

The upper limit z_E of the Ekman layer is assumed to be at the first zero of the v-component of the velocity vector, equation (11), i.e., where it is

$$0 = \sqrt{2} e^{-\frac{z_E - z_P}{D_E}} \sin\psi_E \sin\left(\frac{z_E - z_P}{D_E} + \frac{\pi}{4} - \psi_E\right). \tag{12}$$

The argument of the second sine has to be π and one obtains

$$z_E = z_P + D_E\left(\psi_E + \frac{3}{4}\pi\right).$$

Substitution of D_E yields

$$z_E - z_P = \sqrt{2\frac{\kappa u^* z_P}{f_c}}\left(\psi_E + \frac{3}{4}\pi\right).$$

Assuming that the relative height of the Prandtl layer is given, e.g., $z_P = \alpha z_E$, $\alpha = \frac{1}{40}$, one obtains for the Ekman layer

$$z_E = \frac{2\alpha}{(1-\alpha)^2} \frac{\kappa u^*}{f_c}\left(\psi_E + \frac{3}{4}\pi\right)^2.$$

In order to determine an approximation for z_E one can use the theoretical Ekman angle[c] $\psi_E = \frac{\pi}{4}$ and gets

$$z_E = \frac{2\alpha}{(1-\alpha)^2}\frac{\kappa u^*}{f_c}\pi^2.$$

At the upper limit of the Prandtl layer $z = z_P$ the velocity has to be continuous and one obtains using equation (8) and equation (11)

$$\frac{u^*}{\kappa}\ln\frac{z_P+z_0}{z_0}\cos\psi_E = u_g\left[1-\sqrt{2}\sin\psi_E\cos\left(\frac{\pi}{4}-\psi_E\right)\right],$$
$$\frac{u^*}{\kappa}\ln\frac{z_P+z_0}{z_0}\sin\psi_E = u_g\sqrt{2}\sin\psi_E\sin\left(\frac{\pi}{4}-\psi_E\right).$$

The absolute value of the geostrophic wind u_g is determined using the first equation

$$u_g = \frac{\frac{u^*}{\kappa}\ln\frac{z_P+z_0}{z_0}\cos\psi_E}{1-\sqrt{2}\sin\psi_E\cos\left(\frac{\pi}{4}-\psi_E\right)}.$$

Since the wind vector is usually measured in the Prandtl layer, it is convenient to rotate the coordinate system by the angle ψ_E such that the velocity in the Prandtl layer is parallel to the x-axis. The rotation matrix is

$$\begin{pmatrix} \cos\psi_E & \sin\psi_E \\ -\sin\psi_E & \cos\psi_E \end{pmatrix}.$$

The geostrophic wind and the velocity in the Prandtl layer than have the coordinates

$$\boldsymbol{u}_g = u_g\begin{pmatrix} \cos\psi_E \\ -\sin\psi_E \end{pmatrix}, \quad \boldsymbol{u}_P = \frac{u^*}{\kappa}\ln\frac{z+z_0}{z_0}\begin{pmatrix} 1 \\ 0 \end{pmatrix}.$$

The wind direction φ_W can be taken into account by a similar rotation.

3.4.3 The free atmosphere

In the free atmosphere above the Ekman layer, $z > z_E$, the velocity is assumed to be constant and equal to the value at the top of the Ekman layer $\boldsymbol{u}_E(z_E)$.

3.4.4 The Stability Classes of the Atmosphere

Representative temperature gradients and Ekman angles of the atmosphere can be determined on basis of so-called stability classes of the atmosphere found, e.g., in the german guide-line TA-Luft[4]. For the present calculations, the following parameters have been recommended[8]:

Class	γ_P	γ_E	γ_F	ψ_E
I-II-stable	0.1	0.05	-0.0065	$40°$
III/1-III/2-neutral	-0.01	-0.01	-0.0065	$30°$
IV-V-labile	-0.02	-0.01	-0.0065	$20°$

[c]An Ekman angle of $\psi_E = \frac{\pi}{4}$ assumes that no Prandtl layer is present.[5] This approximation seems to be justified here since the thickness of the Prandtl layer is usually small against the thickness of the Ekman layer.

4 VALIDATION OF RAY TRACING

In order to verify that the ray tracing algorithm works correctly and to illustrate the effects of flow on the noise footprints of a monopole source we compare the solutions obtained with the ray tracing algorithm to the results obtained with an analytical solution for a monopole source. For the derivation of the analytical solution for the monopole the reader is referred to appendix A.

4.1 Stationary source

The simplest case is that of a stationary source in a moving flow. In figures 2(a) and 2(b) the results obtained with the analytical solution are shown for the cases of no flow and uniform flow with a flow Mach number of $M_f = 0.176$, which is typical for a helicopter in fast forward flight. The direction of the flow is from left to right, parallel to the x-axis. The source is located at $(x, y, z) = (0, 0, 300)m$ and the source strength $q' = 1'$ see appendix A. The sound pressure level (SPL) in decibels is computed in the xy-plane for $z = 0$.

The presence of flow has three effects with different physical origin. The first effect is that the acoustic wave fronts are convected with the flow, this is known as the convective effect. This effect leads to a decrease in amplitude upstream of the source and an increase in amplitude downstream of the source. The second effect is due to convective amplification, which increase the amplitude upstream of the source and decreases the amplitude downstream. By comparing figure 2(a) to figure 2(b) one can see that the SPL contours are shifted upstream (to the left). This indicates that the convective amplification is dominant over the convective effect of the flow. The third effect of flow is due to gradients in the flow velocity or gradients in the speed of sound, which can be caused by temperature gradients. Due to these gradients the acoustic wave fronts can be defracted. Figures 2(c) and 2(d) show the results obtained with the ray tracing algorithm, for the case of no flow and uniform flow. The comparison between the results obtained with the analytical solution and those obtained with the ray tracing algorithm are nearly identical. Additionally in figures 2(f) and 2(g) the SPL along the x-axis is shown for both the analytical solution and the solution obtained with the ray tracing algorithm.

Figure 2(h) shows the SPL along the x-axis for the case of a logarithmic velocity profile. It is clear that the SPL downstream of the source decreases faster with distance to the source compared to the case of no flow and uniform flow.

In figure 2(e) the results of the ray tracing algorithm are shown for the case of a logarithmic velocity profile. The velocity profile is that of the Prandtl layer described in section 3.4.1, with the velocity at the bottom

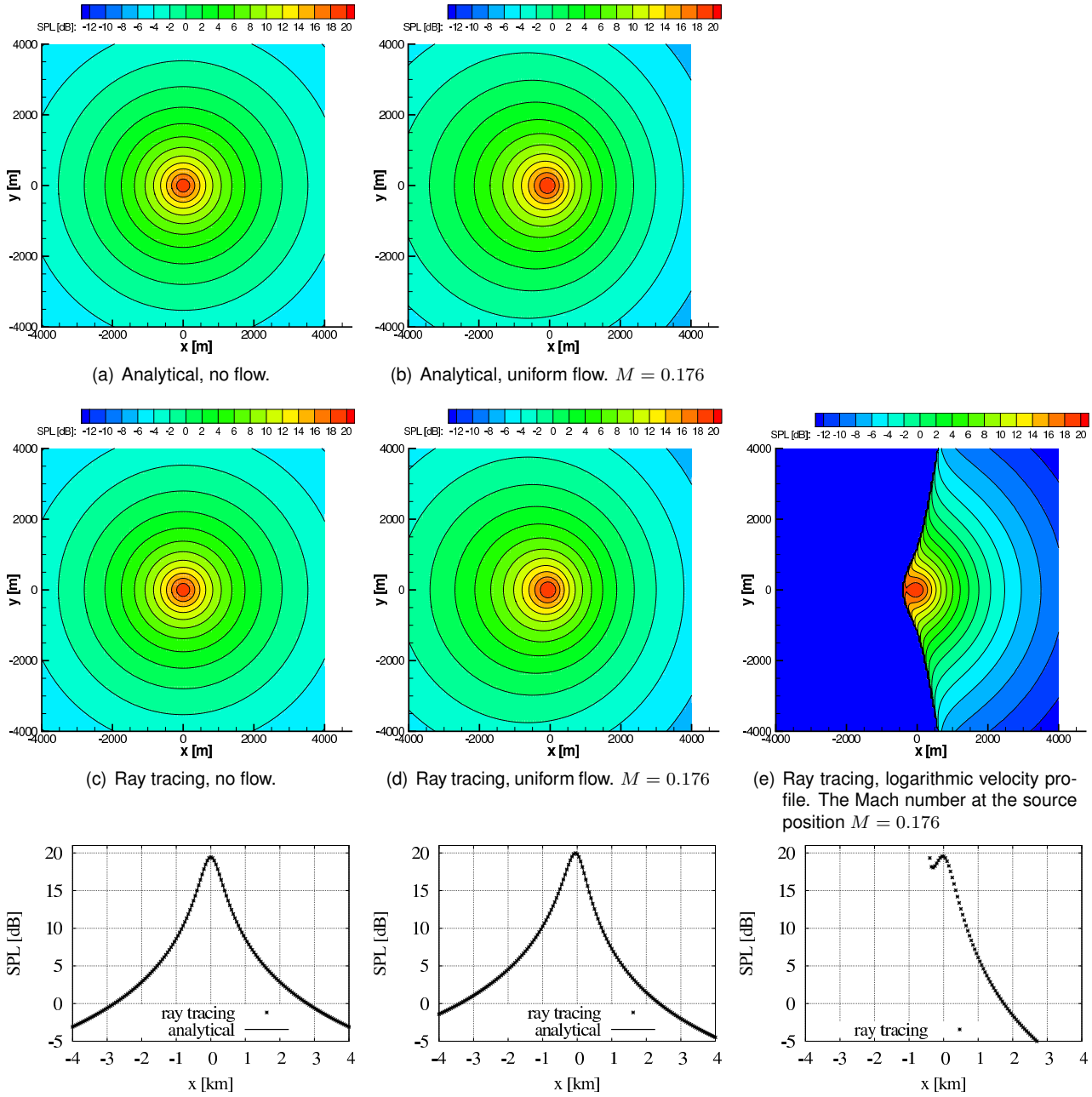

(a) Analytical, no flow.

(b) Analytical, uniform flow. $M = 0.176$

(c) Ray tracing, no flow.

(d) Ray tracing, uniform flow. $M = 0.176$

(e) Ray tracing, logarithmic velocity profile. The Mach number at the source position $M = 0.176$

(f) SPL along the line $y = 0$ for $z = 0$, for the case of no flow.

(g) SPL along the line $y = 0$ for $z = 0$, for the case of uniform flow with $M = 0.176$.

(h) SPL along the line $y = 0$ for $z = 0$, for the case of a logarithmic velocity profile with $M = 0.176$ at $z = 300$ m.

Figure 2: Sound Pressure Level contour plots in xy-plane for $z = 0$. The source is a mass injection monopole and located at $(x, y, z) = (0, 0, 300)$. Analytical results compared to numerical results computed with ray tracing.

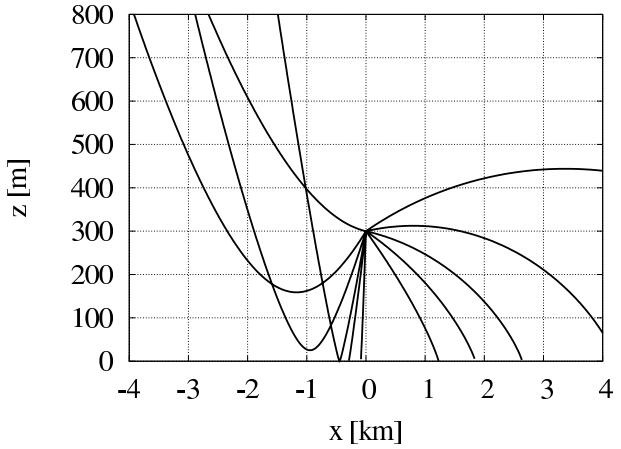

Figure 3: Ray paths for the logarithmic velocity profile used in figure 2(e) in the xz-plane for $y = 0$. The flow direction is from left to right and the source is located at $(x, y, z) = (0, 0, 300)$. Downstream of the source the ray paths are bent downwards. On the upstream side the ray paths are bent upwards and a shadow zone appears for $x < -400$ m.

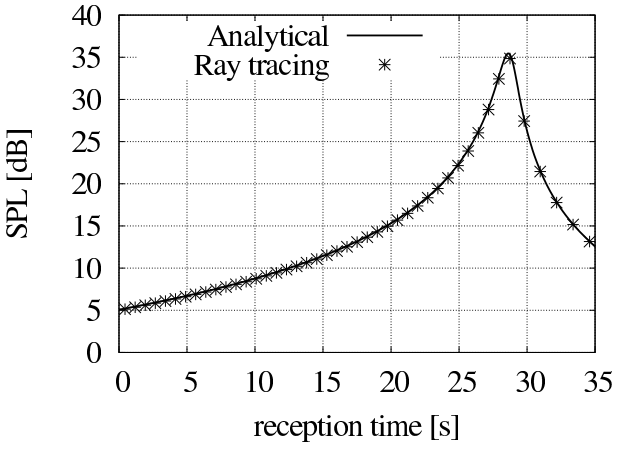

Figure 4: SPL as a function of reception time, for a moving source in a uniform flow. Comparison of ray tracing and analytical solution.

($z = 0$) equal to zero an equal to $M_f = 0.176$ at the source height. This way the convective amplification is the same with respect to the case of uniform flow. As initial conditions for the shooting procedure (see section 3.3) the solution for a straight ray path is used. If the shooting procedures has not met the convergence criteria after a fixed number of iterations it is assumed that the target point is inside the shadow zone and the SPL theoretically should be $-\infty$. However, since $-\infty$ can cause numerical difficulties, the SPL is set to a large negative number ($-1 \cdot 10^3$).

If one compares the case of uniform flow to the case with a logarithmic velocity profile, one sees large difference on the upstream side. Due to the vertical velocity gradient in the flow field the wave fronts are defracted upward on the upstream side and downward on the downstream side. A number of ray paths in the xz-plane for $y = 0$ are shown in figure 3. The flow conditions are the same as those in figure 2(e). The refraction in the upstream side of the source leads to a shadow zone.

The boundary of the shadow zone is the envelope of the crossing rays and called a caustic. At caustics the pressure amplitude of the rays become infinite and the simple ray-theory breaks down. It should be noted, however, that the pressure in the shadow zone drops exponentially away from the caustic[17;9], and the error neglecting it should not be too large. Special approximations can be made there which allow to continue the ray-tracing solution, see, e.g., the references[13;10]. On the downstream side of the source the SPL values are smaller compared to the case of no wind.

The presence of a temperature gradients can also cause bending of the wave fronts. As a rule of thumb the temperature usually decreases by 1 degree with every 100 meter increase in height. The typical height during a helicopter approach is several hundreds of meters and thus the typical gradient in the speed of sound is very small. The effects due to the temperature gradient are therefore usually negligible.

4.2 Moving source

In the previous section the SPL noise footprint of a stationary source with and without flow was investigated. In this section we will investigate the case of a moving source.

In order to verify that the travel time of the wave fronts and the amplitude are correctly computed by the ray tracing algorithm, the SPL as a function of time is computed from the analytical solution and compared to the results obtained with the ray tracing algorithm. The position of the source is given by $(x, y, z) = (80t - 2800, 0, 300 - 8.4t)$, which corresponds to a 6 degrees descent at a constant source Mach number of $M_s = 0.23$. The SPL is computed at the listener position $(x, y, z) = (-500, 0, 0)$, which is fixed in time. The flow is uniform in the negative x-direction and has a Mach number $M_f = 8.7 \cdot 10^{-2}$ (which corresponds to 30m/s). The source strength $q' = 1$. Figure 4 shows the SPL as a function of reception time. The agreement between both signals is very good.

In the case of source movement the SPL will be a function of time and space and we can only produce instantaneous SPL footprint contour plots. In order to provide a plot which also contains the time evolution of the SPL signal we choose to compute the sound exposure level (SEL) in order to visualise the noise footprint. If a the shooting procedure failed to converge the SPL is set to $-1 \cdot 10^9$ and the reception time is set to the reception time corresponding to the case of no wind and constant speed of sound.

It must be noted that the SEL has its drawbacks as a noise measurement quantity. The SEL is defined as

$$\text{SEL} = 10\log_{10}\left(\int_{t_0}^{t_1} 10^{\text{SPL}(t)/10}dt\right). \tag{13}$$

The lower time limit t_0 of the integral in equation 13 is defined as the first point where the SPL comes within 10 dB of the peak value and the upper time limit t_1 is defined as the last point within 10 dB of the peak value. As long as there is a peak in SPL value that is 10 dB higher than the lowest value of the SPL the SEL value obtained is independent of the length of the SPL signal. However, if for instance the peak value is less than 10 dB higher than the lowest value of the SPL then the lower and upper time limit are the start and end time of the SPL signal and consequently the SEL value becomes a function of the measurement time, which is undesirable. The metric EPNL, that is often used for certification, also suffers from this problem. Normally the SEL is computed from a A-weighted SPL signal. In this section we choose not to apply the A-weighting since we use a source with one frequency.

Now that the ray tracing algorithm has been validated with the analytical solution for a monopole we can start using it to investigate more practical cases. We now consider a monopole traveling along a 6 degrees descending path from 300 m height to 0 m height with a constant velocity of 30 m/s. The wind velocity profile is the Prandtl layer with a velocity of 0 m/s at the bottom $z = 0$ and 6 m/s at a height of $z = 10$ m. The source strength $q' = 1$. Although we use a constant velocity the Doppler amplification factor will still change due to a changing velocity seen by the source as it descents to the ground. Figures 5(a) to 5(d) show the SEL footprints in the xy-plane for $z = 0$ for different wind directions and for the case of no wind. The flight path is indicated by the pink dashed line and the arrow. Figure 5(b) serves as a reference and corresponds to the footprint in the case of no wind. It is worth mentioning that the maximum value of the SEL does not occur at $(x, y, z) = (0, 0, 0)$, however, it occurs to the left of it. This is due to the way in which the SEL is computed. To the right of the landing point the SPL value always increases as a function of time, as the source is always approaching these points.

Figure 5(a) shows the SEL footprint in the case of a tail wind, which corresponds to a wind blowing in the positive x-direction. The irregular contours are caused by caustics near the shadow zone boundary, which can cause a large local peak in sound pressure level and thereby affects the time limits of the integral in equation 13.

Figure 5(c) shows the SEL footprint in the case of wind blowing in the negative x-direction, which corresponds to a head wind seen by the source. The influence of the shadow zone causes a cone like shape of the noise footprint.

Figure 5(d) shows the footprint for the case of a side wind blowing in the positive y-direction. The influence of the shadow zone is clearly visible as the oblique boundary. The oblique boundary is mainly caused by the oblique shadow boundary due to the side wind (see the SPL footprint in figure 2(e) and imagine it rotated 90 degrees in counter clockwise direction). Also as the source moves closer to the ground and deeper into the logarithmic velocity profile, the shadow zone boundary moves closer to the source. Outside of the shadow zone the footprint shows lower levels of the SEL compared to the case of no wind, although the shape of the contours is little affected.

Overall it can be concluded that the influence of wind has a noticeable effect in the region upstream of the source due to the shadow zone. However, up to a distance of 500 m left and right of the flight path the contours are not so much affected and hence there the effect of wind on the SEL footprint is small. At larger distances from the flight path the general effect of wind is to lower the SEL noise footprint levels.

It must be noted that the shooting procedure is not always successful in finding the ray path, even though it physically exists. Especially when the source is located close to the ground and the distance to the target point on the ground is large, the shooting procedure has difficulties to converge. In this case small deviations in the emission angles at the source can result in large deviations at the end point, which yields an ill posed problem.

5 HELICOPTER APPROACH NOISE FOOTPRINT PREDICTION WITH WIND

In this section we present numerical results obtained with the use of the computational chain SELENE with the integrated ray tracing and the aeroacoustic database for the EC135-ACT/FHS helicopter.

In order to protect manufacturer interests the absolute values of the contour plots are not published. However, the absolute values of the contours are the same for every plot shown in this section.

As already mentioned in the introduction, the effect of wind can be split into those due to changes in flight conditions (and therefore changes in the acoustic sources) and those due to changes in the propagation of sound through the atmosphere. The change in flight conditions is covered in SELENE by providing the flight mechanics code with the wind conditions at the helicopter position. This will lead to values for the attitude angles, thrust coefficient, advance ratio and tip path plane angle that are different compared to those obtained in the case of no wind.

In real flight tests it is difficult to discriminate between differences due to propagation effects and differences due to changes in flight conditions because both effects occur simultaneously. With the computa-

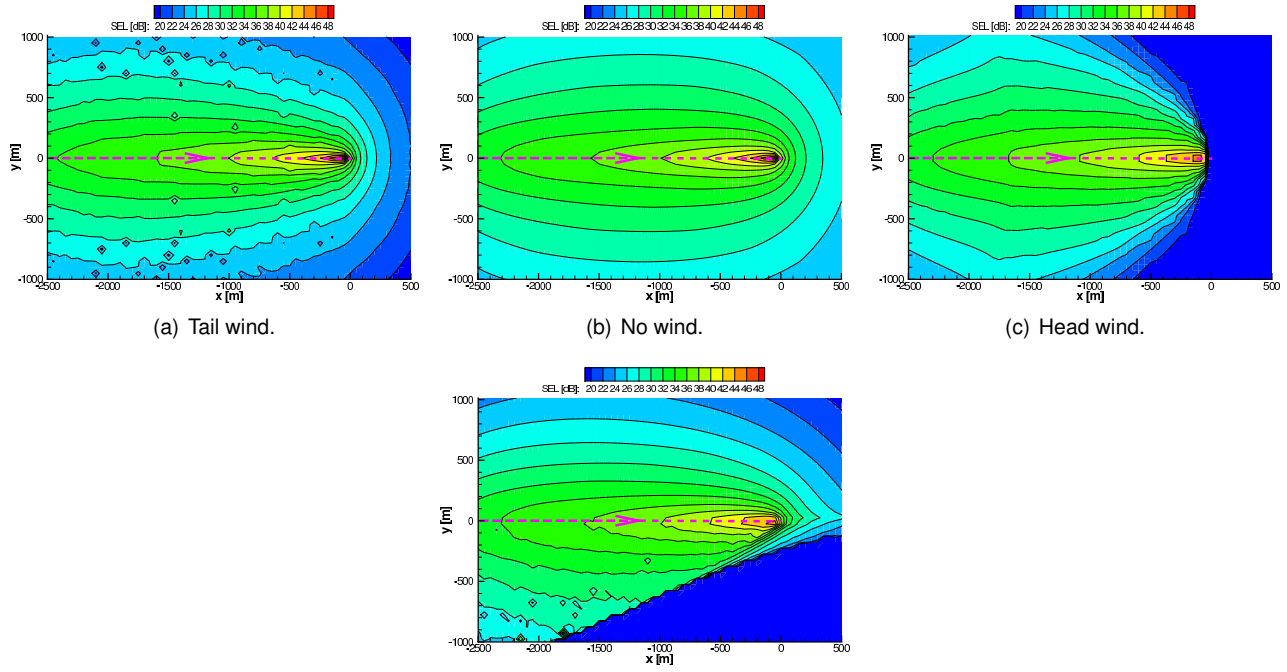

(a) Tail wind. (b) No wind. (c) Head wind.

(d) Side wind.

Figure 5: Sound Exposure Level contour plots in xy-plane for $z = 0$ for different wind directions. The source is a mass injection monopole and follows a 6 degrees descending path.

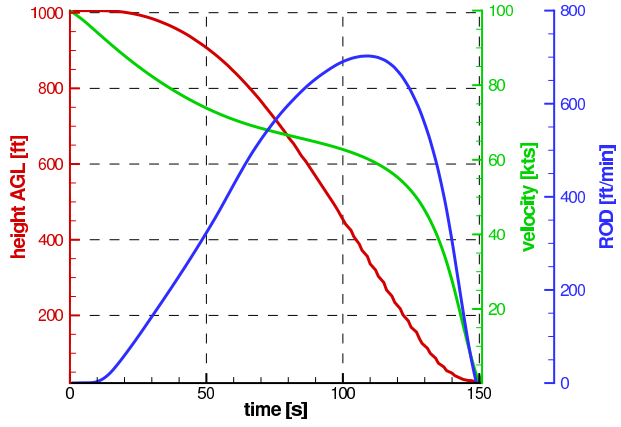

Figure 6: Height above ground level in feet, velocity in the horizontal plane in knots and rate of descent (ROD) in feet per minute as a function of time.

tional chain it is, however, possible to investigate both effects separately.

As flight procedure we choose the same flight procedure that was used in previous publications as a reference landing procedure [16;7]. Details of this flight procedure are presented in figure 5, it shows the height above ground level (AGL) in feet, flight velocity in the horizontal plane in knots and the rate of descent (ROD) in feet per minute as a function of time. It was chosen to present the parameters of the flight procedure in the units that are common in the literature and legislation on flight procedures. The benefit of using time as the independent variable is that time is always monotonically increasing, while the distance to the landing point might not be, especially for three dimensional flight paths.

The SEL noise footprints of the procedure shown in figure 5 are presented in figure 7 for different conditions. In the computations the effect of ground reflection has not been taken into account since no comparison with experimental data is made. The footprints are presented with A-weighting as SEL in dBA. The difference between the contour levels is 5 dBA. The flight path starts at $(x, y, z) = (-5100, 0, 304)$ m with a velocity of 100 knots, is parallel to the x-axis and ends at the landing point at $(x, y, z) = (0, 0, 0)$. The wind velocity profile is the three layer atmospheric model as described in section 3.4, with a wind velocity of 5 m/s at a height of 10 m above ground level and 15 m/s at 300 m above ground level. The atmospheric stability class used is *"III/1-III/2-neutral"*. For these condition the Prandlt layer has a height of 23 meters and the Ekman layer extends to 945m. Note that due to the spiraling effect in the Ekman layer the wind direction changes with height, such that at 300 m height the wind direction is rotated by 14 degrees. The number of microphones in the y-direction is 11 and 16 in the x-direction, which yields a total of 176 microphones.

The noise footprint in the case of no wind is shown in figure 7(a) and can be considered as a reference to assess the influence of different wind effects. In all plots the maximum value of the SEL occurs before (left

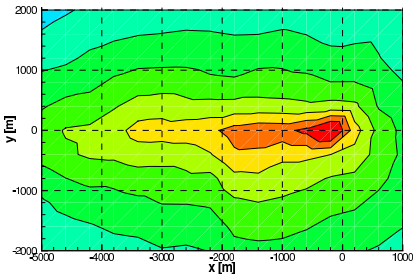

(a) No wind.

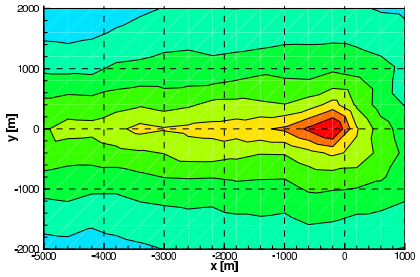

(b) Tail wind. Wind influence on flight mechanics only, no wind effect on propagation of sound.

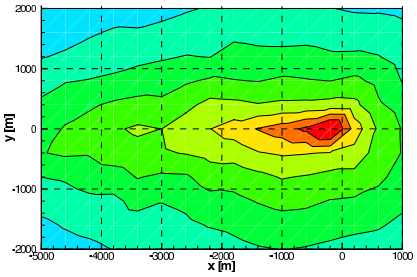

(c) Side wind. Wind influence on the flight mechanics only, no wind effect on propagation of sound.

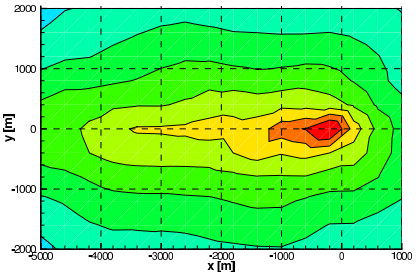

(d) Head wind. Wind influence on flight mechanics only, no wind effect on the propagation of sound.

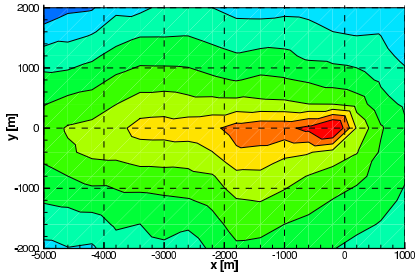

(e) Tail wind. Wind influence on propagation of sound through atmosphere only, no effect of wind on the flight mechanics.

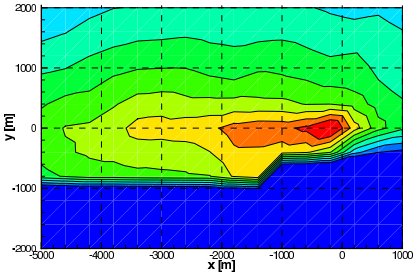

(f) Side wind. Wind influence on propagation of sound through atmosphere only, no effect of wind on the flight mechanics.

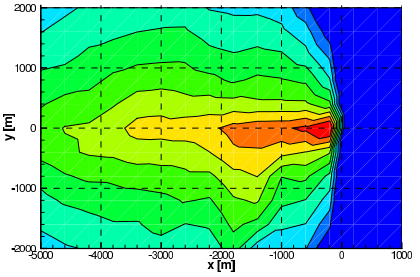

(g) Head wind. Wind influence on propagation of sound through atmosphere only, no effect of wind on the flight mechanics.

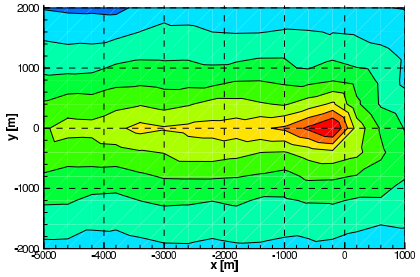

(h) Tail wind. Wind influence on both flight mechanics and propagation taken into account.

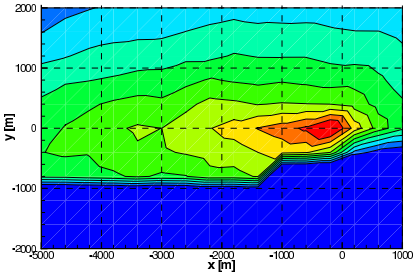

(i) Side wind. Wind influence on both flight mechanics and propagation taken into account.

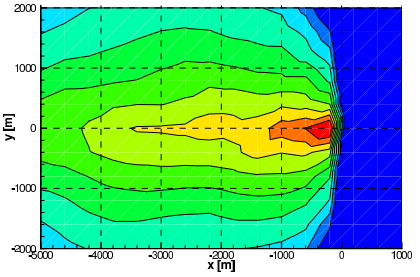

(j) Head wind. Wind influence on both flight mechanics and propagation taken into account.

Figure 7: Sound Exposure Level (SEL) contour plots, for the EC135 in xy-plane for $z = 0$, illustrating the relative importance of the effect of wind on the source due to different flight mechanics and the importance of wind on the propagation of sound through the atmosphere. Details of the flight procedure are shown in figure 5. The landing point is located at $(x, y, z) = (0, 0, 0)$. The difference between the contour levels is 5 dBA. The wind velocity at 10 m above ground is 5 m/s.

of) the landing point at $(x, y, z) = (0, 0, 0)$.

Figures 7(b), 7(c) and 7(d) show the noise footprint in the case of a tail wind, a side wind from below and head wind respectively. Here the influence of wind on the flight mechanics is only taken into account. The effects of wind on the propagation of sound through the atmosphere are not taken into account. This means that the same procedure is flown as for the case of no wind, however, the values of the flight mechanical parameters used for the noise hemisphere selection from the aeroacoustic database (μ, α_{TTP}, C_T) are different from the values obtained in the case without wind. Consequently different noise hemispheres are selected from the aeroacoustic database. In figure 7(b) the tail wind causes the the noise contours before the landing point to become more narrow compared to the case of no wind in figure 7(a). The side wind makes the noise footprint shorter on the inside and the contour values at the outer boundary are lower, as can be seen in figure 7(c). In figure 7(d) little difference is observed compared to the footprint in figure 7(a), only the second highest contour is about a factor two shorter.

The noise footprints where only the influence of wind on the propagation of sound is taken into account are shown in figures 7(e), 7(f) and 7(g). As in figure 5 the contour levels right below the flight path are little affected by the presence of wind. At larger distance, however, the effect of the shadow zone is clearly visible in figures 7(c) and 7(g).

Figures 7(h), 7(i) and 7(j) show the noise footprints in case the influence of wind is fully taken into account (both influence on flight condition and propagation effects), which corresponds to a realistic flight procedure. The noise footprint with a head wind component respresents the most practically relevant case, since a pilot will always prefer to land with head wind.

When comparing figures 7(b) to 7(j) with figure 7(a) it can be concluded that compared to the case of no wind the changes in the contours right below the flight path are mostly affected by changes in flight conditions, i.e. changes in acoustical sources. The contours further away from the flight path are mostly affected by propagation effects. The overall effect of wind is the most significant for a head or side wind component.

6 CONCLUSIONS

The computational chain SELENE for noise footprint prediction has been extended with a ray tracing algorithm to incorporate the effects of wind, wind gradients and temperature gradients. The ray tracing algorithm has been validated by comparison with the analytical solution for a mass injection monopole moving in a uniform flow. The Sound Exposure Level (SEL) footprints have been presented for a moving monopole source and for an EC135 helicopter.

For the case of a stationary source the effect of a wind velocity profile leads to the appearance of a shadow zone. However, for the case of a moving source the shadow zone is also moving and its effect is less pronounced in sound exposure level (SEL) contour plots. The most pronounced effects on the SEL contours is at locations which are inside the shadow zone during the entire movement of the source.

The SEL noise contours right below the flight path are mostly affected by the changes in flight mechanics, i.e., changes in the acoustic sources, while the noise contours further away from the flight path are mostly affected by propagation effects. In general the effect of wind is to lower the SEL noise footprint contour levels and the effect of wind is the most significant for the case of head wind.

The extension of the computational chain can be used in the future to optimise flight procedures where the effects of wind are taken into account. Furthermore the capability to analyse flight experimental data, which was obtained with wind, is enhanced.

7 ACKNOWLEDGMENTS

The research presented in this paper was partly supported by the European Joint Technology Initiative CleanSky, as part of the subtask GreenRotorCraft 5, under grant agreement number CSJU-GAM-GRC-2008-001.

REFERENCES

[1] P. Beaumier, J. Prieur, G. Rahier, P. Spiegel, A. Demargne, C. Tung, J. Gallman, Y. Yu, R. Kube, B. Van der Wall, K.-J. Schultz, W. Splettstoesser, T. Brooks, C. Burley, and J. D.D.Boyd. Effect of higher harmonic control on helicopter rotor blade-vortex interaction noise : prediction and initial validation. Berlin, Germany, October 1994. AGARD 75th Fluid Dynamics Panel Meeting and Symposium on Aerodynamics and Aeroacoustics of Rotorcraft.

[2] B. Benoit, A.-M. Dequin, K. Kampa, W. Von Grünhagen, P.-M. Basset, and B. Gimonet. HOST, a General Helicopter Simulation Tool for Germany and France. Virginia Beach, VA, USA, May 2-4 2000. American Helicopter Society 56th Annual Forum.

[3] L. M. Brekhovskikh and O. A. Godin. *Acoustics of Layered Media II*, volume 10 of *Springer Series on Wave Phenomena*. Springer Verlag, Berlin/Heidelberg/New York, 1999.

[4] Bundesministerium für Umwelt, Naturschutz und Reaktorsicherheit. Erste Allge-

meine Verwaltungsvorschrift zum Bundes-Immissionsschutzgesetz (Technische Anleitung zur Reinhaltung der Luft – TA Luft). Verwaltungsvorschrift, Bundesministerium für Umwelt, Naturschutz und Reaktorsicherheit, 2002.

[5] D. Etling. *Theoretische Meteorologie*. Vieweg Verlag, Wiesbaden, 1996.

[6] G. Gopalan and F. H. Schmitz. Flight Path Control of Helicopter Blade-Vortex-Interaction Noise in the Prescence of Wind. Washington, DC, USA, May 9-11 2001. American Helicopter Society 57th Annual Forum.

[7] F. Guntzer, P. Spiegel, and M. Lummer. Genetic Optimization of EC-135 Noise Abatement Flight Procedures using an Aeroacoustic Database. Hamburg, Germany, September 22-25 2009. 35th European Rotorcraft Forum.

[8] D. Heimann. Schalldämpfung auf Grund der Meteorologie- und Bodeneinflüsse. Private Communication, 2003.

[9] U. Ingard. Atmospheric acoustics. NASA Contract NAw-6516, Massachusetts Institute of Technology, December 1959.

[10] Y. W. Lam. An analytical model for turbulence scattered rays in the shadow zone for outdoor sound propagation calculation. *The Journal of the Acoustical Society of America*, 125:1340–1350, 2009.

[11] A. Le Duc, P. Spiegel, F. Guntzer, M. Lummer, H. Buchholz, and J. Götz. Simulation of Complete Helicopter Noise in Maneouver Flight using Aeroacoustic Flight Test Database. Montréal, Canada, April 26 - May 1 2008. Americal Helicopter Society 64th Annual Forum.

[12] Y. Liu, A. P. Dowling, and A. R. Quayle. Numerical simulation of beamforming correction for dipole source identification. Number BeBeC-2008-05. 2nd Berlin Beamforming Conference, 19-20 February 2008.

[13] E. M. Salomons. Caustic diffraction fields in a downward refracting atmosphere. *The Journal of the Acoustical Society of America*, 104:3259–3272, 1998.

[14] J. Schulten. Computation of aircraft noise propagation through the atmospheric boundary layer. University of Adelaide, Australie, December 15-18 1997. 5th International Congress on Sound and Vibration.

[15] P. Spiegel, H. Buchholz, and M. Pott-Pollenske. Highly Instrumented BO105 and EC135-FHS Aeroacoustic Flight Tests including Maneuver Flights. Grapevine, TX, USA, June 1-3 2005. Americal Helicopter Society 61th Annual Forum.

[16] P. Spiegel, F. Guntzer, A. Le Duc, and H. Buchholz. Aeroacoustic Flight Test Data Analysis and Guidelines for Noise-Abatement-Procedure Design and Piloting. Liverpool, UK, September 16-19 2008. 34th European Rotorcraft Forum.

[17] D. C. P.-B. und Uno Ingard. Tentative method for calculation of the sound field about a source over ground considering diffraction and scattering into shadow zones. NACA Research Memorandum 57B25, National Advisory Committee for Aeronautics, April 1957.

[18] Y. Yu, C. Tung, B. van der Wall, H.-J. Pausder, C. Burley, T. Brooks, P. Beaumier, Y. Delrieux, E. Mercker, and K. Pengel. The HART-II Test: Rotor Wakes and Aeroacoustics with Higher-Harmonic Pitch Control (HHC) Inputs – The Joint German/French/Dutch/US Project. Montreal, Canada, June 2002. American Helicopter Society 58th Annual Forum.

A ANALYTICAL SOLUTION FOR A MOVING MONOPOLE IN UNIFORM FLOW

The acoustic pressure perturbation p in a moving medium with uniform velocity $\boldsymbol{U}_\infty$ and constant speed of sound c_0 is governed by the convected wave equation

$$\frac{1}{c_0^2}\frac{D^2p}{Dt^2} - \nabla^2 p = Q, \quad \text{with} \quad \frac{D}{Dt} = \frac{\partial}{\partial t} + \boldsymbol{U}_\infty \cdot \nabla. \tag{14}$$

Here time is denoted by t, and $\boldsymbol{x}$ is the spatial coordinate. For a mass injection source q, whose position is given by $\boldsymbol{x}_s(t)$, we have $Q = \frac{D}{Dt}\left[q(t)\delta(\boldsymbol{x} - \boldsymbol{x}_s(t))\right]$. Where δ denotes the Dirac delta function. Equation 14 can be solved analytically by making use of the free field Green's function for the convected wave equation

$$G(\boldsymbol{x}, t|\boldsymbol{\xi}, \tau) = \frac{\delta\left(\tau - t + \frac{|\boldsymbol{x}-\boldsymbol{\xi}-\boldsymbol{U}_\infty(t-\tau)|}{c_0}\right)}{4\pi|\boldsymbol{x} - \boldsymbol{\xi} - \boldsymbol{U}_\infty(t-\tau)|}. \tag{15}$$

The Green's function establishes the relation between a needle pulse emitted at the source location $\boldsymbol{\xi}$ at the emission time τ and the listener position $\boldsymbol{x}$ at the reception time t. The solution is obtained by convoluting the right hand side of equation 14 with the Green's function and integrating over all space and time

$$p(\boldsymbol{x}, t) = \int_{-\infty}^{+\infty}\int_{V_\infty} G\left(\frac{\partial}{\partial\tau} + \boldsymbol{U}_\infty \cdot \nabla_\xi\right) \cdot \left[\delta\left(\boldsymbol{\xi} - \boldsymbol{\xi}_0(\tau)\right) q(\tau)\right] dV(\boldsymbol{\xi}) d\tau. \tag{16}$$

By using the chain rule or partial integration the time and space derivatives can be moved to derivatives of the Green's function. Then the properties of the Green's function $\frac{\partial G}{\partial t} = -\frac{\partial G}{\partial \tau}$ and $\frac{\partial G}{\partial \boldsymbol{x}} = -\frac{\partial G}{\partial \boldsymbol{\xi}}$ are used to move from derivatives in τ and $\boldsymbol{\xi}$ to derivatives in t and $\boldsymbol{x}$ which yields

$$p(\boldsymbol{x},t) = \int_{-\infty}^{+\infty} \int_{V_\infty} \delta\left(\boldsymbol{\xi} - \boldsymbol{\xi}_0(\tau)\right) q(\tau) \frac{\partial G}{\partial t} + \boldsymbol{U}_\infty \cdot \left[\delta\left(\boldsymbol{\xi} - \boldsymbol{\xi}_0(\tau)\right) q(\tau) \nabla_{\boldsymbol{x}} G\right] dV(\boldsymbol{\xi}) d\tau. \tag{17}$$

Now the derivatives can be taken outside the integral and the integration can be performed. The solution for the pressure p at point $\boldsymbol{x}$ and time t, of a moving monopole in a uniform flow is then given by

$$p(\boldsymbol{x},t) = \frac{\frac{dq}{dt} + q\left(\boldsymbol{e}_R \cdot \frac{d\boldsymbol{M}}{dt}\right)(1 - M_R)^{-1}}{4\pi |\boldsymbol{R}| (1 - M_R)^2} + \frac{q c_0 \left(M_R - \boldsymbol{M}^2\right)}{4\pi |\boldsymbol{R}|^2 (1 - M_R)^3}, \tag{18}$$

with

$$\boldsymbol{R} = \boldsymbol{x} - \boldsymbol{x}_s(\tau) - \boldsymbol{U}_\infty (t - \tau), \tag{19}$$

$$\boldsymbol{M} = \frac{1}{c_0} \left(\frac{d\boldsymbol{x}_s}{dt} - \boldsymbol{U}_\infty \right), \tag{20}$$

$$\boldsymbol{e}_R = \boldsymbol{R} / |\boldsymbol{R}|, \tag{21}$$

$$M_R = \boldsymbol{e}_R \cdot \boldsymbol{M}. \tag{22}$$

The position of the source is given by $\boldsymbol{x}_s(t)$ and the flow velocity is given by $\boldsymbol{U}_\infty$. Here τ is the so called emission time and is obtained by solving the equation $t - \tau - |\boldsymbol{R}|/c_0 = 0$. As usual all the terms on the right hand side of equation 18 are to be evaluated at the emission time τ. It is important to realise that the source movement and velocity can be arbitrary, in contrast to the flow velocity, which must be constant. For a flow velocity other than constant it is not possible to derive a convected wave equation.

The first term on the right hand side of equation 18 is known as the far field term and the second term is known as the near field term. Since the ray equations correspond to the high frequency limit, there exists no near field. For comparison and validation we should therefore leave out the near field term.